

Phase transition in the magnetocrystalline anisotropy of tetragonal Heusler alloys: Rh₂TSb, $T = \text{Fe, Co}$

Gerhard H. Fecher,* Yangkun He, and Claudia Felser
Max-Planck-Institute for Chemical Physics of Solids, D-01187 Dresden, Germany
 (Dated: March 18, 2022)

This work reports on first principles calculations of the electronic and magnetic structure of tetragonal Heusler compounds with the composition Rh₂Fe_{*x*}Co_{1-*x*}Sb ($0 \leq x \leq 1$). It is found that the magnetic moments increase from 2 to 3.4 μ_B and the Curie temperature decreases from 500 to 464 K with increasing Fe content *x*. The 3*d* transition metals make the main contribution to the magnetic moments, whereas Rh contributes only approximately 0.2 μ_B per atom, independent of the composition. The paper focuses on the magnetocrystalline anisotropy of the borderline compounds Rh₂FeSb, Rh₂Fe_{0.5}Co_{0.5}Sb, and Rh₂CoSb. A transition from easy-axis to easy-plane anisotropy is observed when the composition changes from Rh₂CoSb to Rh₂FeSb. The transition occurs at an iron concentration of approximately 40%.

Keywords: Electronic structure, Magnetocrystalline anisotropy, Intermetallic compounds, Rh₂FeSb, Rh₂CoSb

I. INTRODUCTION

Permanent or hard magnets are made of bulk materials with strong anisotropy, which may be based on magnetocrystalline, shape anisotropy, or both. In magnets with magnetocrystalline anisotropy, there should be only one easy crystal axis of magnetisation so that the anisotropy is uniaxial. Such an uniaxial magnetocrystalline anisotropy is found, for example, in tetragonal or hexagonal systems. Heusler alloys are compounds with formula $T_2T'M$, where *T* and *T'* are transition metals, and *M* is a main group element. Some of these compounds and alloys crystallise in tetragonal structure; however, most of them have a cubic crystal structure. One advantage of Heusler compounds is that most of them do not contain rare earth elements; rather, the magnetic properties are provided by 3*d* transition metals. Many tetragonal Heusler alloys are Mn-based, and several exhibit structural martensite–austenite phase transitions. In particular, in the *inverse* structures with space group $I\bar{4}m2$, the magnetic moments of the Mn atoms exhibit antiparallel coupling. Thus, these alloys are generally ferrimagnets with low saturation magnetisation. The Rh₂*TM* alloys (*T'* = V, Mn, Fe, Co; *M* = Sn, Sb) crystallise in a regular tetragonal structure with space group $I4/mmm$ and are expected to exhibit uniaxial anisotropy when the 3*d* transition metals have large moments.

Experiments on the crystal structure and magnetic properties of Rh₂-based Heusler compounds were reported by Dhar *et al.* [1], who observed a tetragonal structure and a magnetic moment of 1.4 μ_B in the primitive cell. A Curie temperature of approximately 450 K was measured. Further, Fallev *et al.* recently reported *ab initio* calculations for many tetragonal Heusler compounds (including Rh₂FeSb and Rh₂CoSb) [2]. This work proposed that thin films of Rh₂CoSb exhibit uni-

axial, perpendicular anisotropy with the easy direction along the *c* ([001]) axis. Experiments and calculations both suggest that Rh₂CoSb might be suitable hard magnetic material with uniaxial anisotropy. However, the constituent elements, in particular Rh, might be too expensive for applications where bulk materials are needed, for example, permanent magnets in electric engines. However, the cost of the materials is not as important for thin film applications, for example, magnetic recording media or magnetoelectronic memory devices.

We recently reported experiments on the magnetic properties of Rh₂CoSb [in print, will be added later]. It was found that Rh₂CoSb has uniaxial anisotropy, where *c* is the *easy* axis. The present work describes theoretically the magnetic properties of Rh₂CoSb, its sister compound Rh₂FeSb, and alloys with mixed Co_{1-*x*}Fe_{*x*} composition.

II. DETAILS OF THE CALCULATIONS

The electronic and magnetic structures of Rh₂TSb ($T = \text{Fe, Co}$) were calculated using WIEN2k [3–5] and SPRKKR [6, 7] in the local spin density approximation. In particular, the generalised gradient approximation of Perdew, Burke, and Ernzerhof [8] was used to parametrise the exchange correlation functional. A *k*-mesh based on $126 \times 126 \times 126$ points of the full Brillouin zone was used for integration when the total energies were calculated to determine the magnetocrystalline anisotropy (see also Appendix C). The calculations are described in greater detail in References [9, 10]. The spin spirals and magnons were calculated according to the schemes described in References [11] and [12], respectively. Calculations for the disordered or off-stoichiometric compounds with mixed site occupations were performed using SPRKKR and the coherent potential approximation (CPA) [13] in the full potential mode. The CPA allows the simulation of random site occupation by different elements. Complications arising in the

* fecher@cphys.mpg.de

calculation of the magnetic anisotropy energies are discussed in detail by Khan *et al.* [14], who compared results obtained using WIEN2k and SPRKKR.

The basic crystal structure of the tetragonal Heusler compounds [prototype, Rh_2VSn ; $tI8$; $I4/mmm$ (139) dba] is shown in Figure 1(a). The atoms are located in the ferromagnetic structure on the 4d, 2b, and 2a Wyckoff positions of the centred tetragonal cell. The magnetic order changes the symmetry, and the resulting magnetic space group for collinear ferromagnetic order with moments along the c axis is $I4/m'm'm'$ (139.537), where $'$ is the spin reversal operator [15]. The symmetry is reduced to that of space group $I m'm'm$ (71.536) when the magnetisation \vec{M} is along the a axis ($[100]$) or $F m'm'm$ (69.524) for $\vec{M} \parallel [110]$.

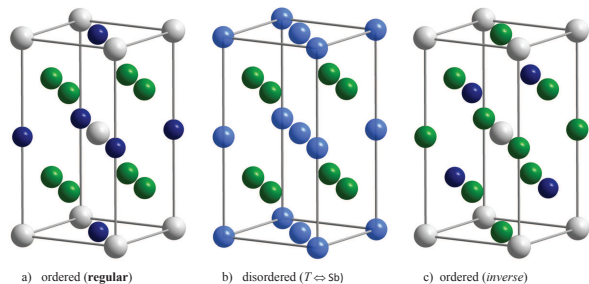


FIG. 1. Crystal structure of Rh_2TSb ($T = \text{Fe}, \text{Co}$). In the well-ordered regular structure (a), the sites of the lattice with space group $I4/mmm$ (139) are occupied as follows: 4d (0 1/2 1/4), Rh; 2b (0 0 1/2), T ; and 2a (0 0 0), Sb. In the disordered structure (b), the T and Sb atoms are randomly distributed on the 2b and 2a sites. The *inverse* tetragonal structure is shown in (c) for comparison.

The electronic structure and magnetic properties were calculated using the optimised lattice parameters. As starting point, the lattice parameters of two alternative structures were optimised using WIEN2k. In addition to the regular Heusler structure described above, the inverse structure with space group $I\bar{4}m2$ (119) $dbca$ was assumed. In this structure, the positions of the Co atom and one of the Rh atoms are interchanged. Spin-orbit interaction was considered owing to the high Z values of Rh and Sb. Note that the spin-orbit interaction is an intrinsic property in the fully relativistic SPRKKR calculations, which solve the Dirac equation. The results of the optimisation are summarised in Table I. The regular structure is found to have lower energy; it thus describes the ground state. The energy difference compared to the inverse structure is approximately 430 meV. The formation enthalpy is calculated as $\Delta H_f = E_{tot} - (2E_{\text{Rh}} + E_{\text{Co}} + E_{\text{Sb}})$, that is, the difference between the total energy of the compound in different structures and the sum of the energies of the elements in their ground state structure. The formation enthalpy is clearly lower for the regular structure than for the inverse tetragonal structure. Note that the formation enthalpy is even lower (-220 meV) for the cubic $L2_1$ structure. The calculated lattice param-

eters are in good agreement with experimental values [1]; however, the calculated c value and c/a ratio are approximately 4% larger. This finding might be explained by either a temperature effect or some disorder in the experiment.

TABLE I. Structural properties of Rh_2CoSb . Calculations are performed for the regular (139) and inverse (119) Heusler structures. The lattice parameters (a , c , c/a), formation enthalpy (ΔH_f), and spin magnetic moment m_s of the primitive cell (total experimental magnetic moment) are listed. Experimental values from Reference [1] are shown for comparison. Note that the magnetic moment in this reference is not saturated.

	Calculated		Exp.	
	139	119	here	[1]
a [\AA]	4.0104	3.95	4.0393	4.04
c [\AA]	7.3628	7.56	7.1052	7.08
c/a	1.836	1.91	1.759	1.75
ΔH_f [meV]	-754	-325		
m_s [μ_B]	2.04	1.79	2.36	1.4
T_C [K]			450	450

III. RESULTS AND DISCUSSION

A. Electronic and magnetic structure of Rh_2CoSb

The calculated electronic structure of Rh_2CoSb in the regular tetragonal Heusler structure is illustrated in Figure 2 in terms of the band structure and density of states ($n(E)$). The relativistic bands, spin-resolved total density of states, and its atomic contributions are shown. The electronic structure is calculated in the full relativistic mode by solving the Dirac equation. The band structure from semi-relativistic calculations is shown in the Appendix.

Both rhodium and cobalt contribute to the magnetic moment of the compound. The spin and orbital magnetic moments are $m_s^{\text{Co}} = 1.656 \mu_B$ and $m_l^{\text{Co}} = 0.139 \mu_B$ for cobalt and $m_s^{\text{Rh}} = 0.206 \mu_B$ and $m_l^{\text{Rh}} = 0.007 \mu_B$ for rhodium, respectively. The overall magnetic moment (spin plus orbital) of the primitive cell is $m_{\text{tot}} = 2.188 \mu_B$. The orbital moment of the Co atoms makes a remarkably large contribution.

The real space charge and spin distributions are shown in Figure 3. The charge density ($\sigma(r)$) of the atoms has no striking shape. It appears to be nearly spherical but still reflects the two- or fourfold symmetry. As expected, most of the electrons are close to the ion cores. By contrast, the spin or magnetisation density ($\sigma(r)$) has a much more pronounced shape depending on the plane. In particular, in the (110) plane, it has a distinct butterfly shape. The spin density is positive at both the Co and Rh atoms. It is clearly higher near the Co atoms than

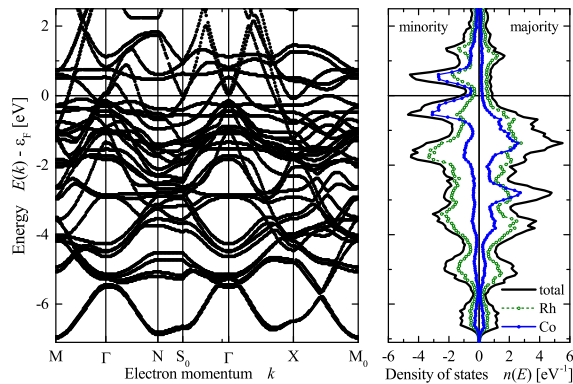


FIG. 2. Electronic structure of Rh_2CoSb (I). Shown is the fully relativistic band structure together with the total and site (Rh and Co) specific, spin-resolved densities of states.

near the Rh atoms, which ultimately gives Co a higher magnetic moment. The magnetisation density of the Rh atoms is aligned along the magnetisation direction and points somewhat toward the nearest Co atoms.

1. Magnetic anisotropy

Further, the directional dependence of the magnetisation was investigated to explain the collinear magnetic order in detail. In particular, the total energy was calculated for cases where the magnetisation points along different crystallographic directions. The obtained energy differences make it possible to determine the magnetocrystalline anisotropy (see also Appendix C).

In the magnetic anisotropy of Rh_2CoSb , the *easy* axis is along the c ([001]) axis. The simple second-order uniaxial anisotropy constant is $K_u = 1.37 \text{ MJ/m}^3$ (see Equations (C1) and (C2) in Appendix C1). This results in an anisotropy field of $\mu_0 H_u \approx 2.4 \text{ T}$. A more detailed analysis reveals that the simple second-order anisotropy constant K_u is not sufficient to describe the magnetocrystalline anisotropy, as discussed in Section III D.

Further, the dipolar magnetocrystalline anisotropy was calculated as described in Appendix C3 and was found to be $\Delta E_{\text{dip,aniso}} = 0.09 \mu\text{eV}$. The positive value indicates an easy dipolar direction along the [001] axis. The dipolar anisotropy is rather small compared to the anisotropy calculated from the total energy. Here, it was calculated for a sphere with a radius of 30 nm. The results for other shapes will be different, resulting in a distinct shape anisotropy. In particular, in thin films, the dimension perpendicular to the film is much smaller than the dimensions in the film plane. Therefore, the summation in Equation (C16) becomes a truncated sphere that is strongly anisotropic, and a pronounced thin film anisotropy appears. This thin film anisotropy will also be affected by the magnetic moments, which are different at

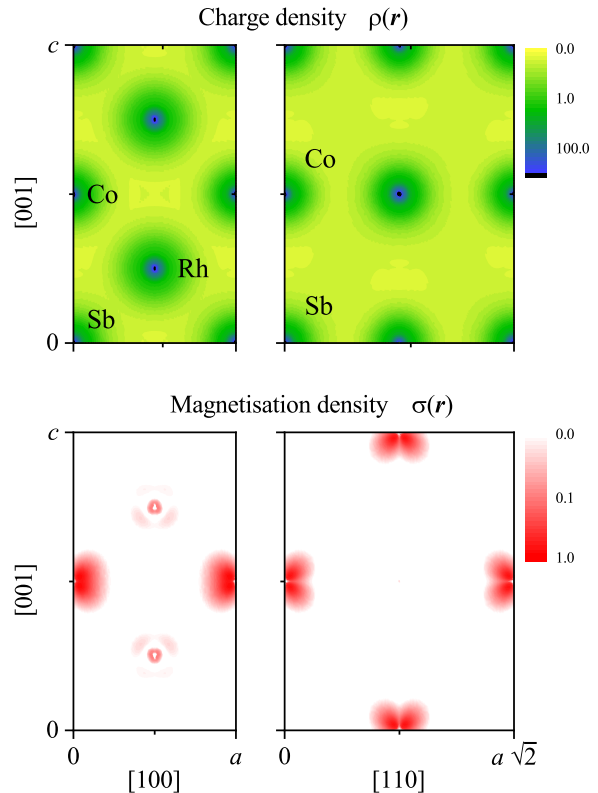


FIG. 3. Electronic structure of Rh_2CoSb (II). Fully relativistic charge ($\rho(r)$) and spin ($\sigma(r)$) distributions for the (001) and (110) planes are shown. The calculation is for $m \parallel c$, that is, the magnetisation points along [001] according to the *easy axis* behaviour of the magnetic anisotropy. (Note: colour bars are in atomic units.)

interfaces and surfaces from that at the centre layers of the film.

2. Spiral spin order

The energy of the spin spirals was calculated to search for non-collinear magnetic order. The spin spirals were calculated for different directions and different cones. In planar spirals, the spins are perpendicular to the propagation direction. Figure 4 compares the energies of planar spirals along the high-symmetry directions.

The spirals along [100] or [110] propagate in the four-fold plane, whereas the spiral in the [001] direction propagates along the c axis. In all cases, the lowest energy is observed at $q = 0$. The magnetic moment of the Co atoms varies by approximately 17% at maximum. The magnetic moment of the Rh atoms decreases with increasing q and vanishes at the border, independent of the propagation direction of the spiral.

The spin direction was assumed to be perpendicular

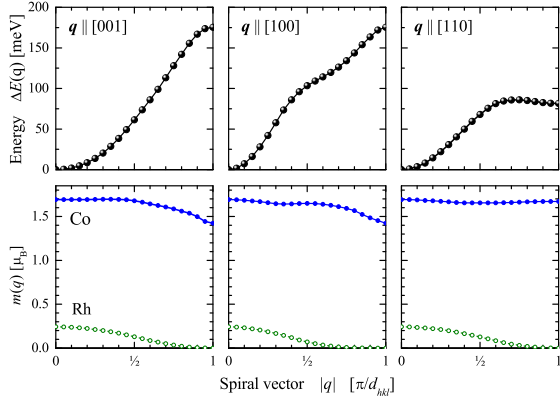


FIG. 4. Planar spin spirals in Rh_2CoSb . The spiral energies are given with respect to $q = 0$, that is, $\Delta E(q) = E(q) - E(0)$. The behaviour of the magnetic moment $m(q)$ is shown for Rh and Co.

to the q vector in the above calculations for planar spirals. Thus, the angle between \vec{q} and the local magnetic moment \vec{m}_i was set to $\Theta = \pi/2$. Next, the spirals were assumed to be conical with $0 < \Theta < \pi/2$ to allow for a more detailed analysis. The calculations were performed for q along [001]. Figure 5 displays the results for conical spirals with various cone angles. The highest energies appear for the planar spiral. The energy at the border of the Brillouin zone ($q = \pi/c$) exhibits a sine dependence. Thus, it vanishes in the antiferromagnetic state. The behaviour of the local magnetic moments suggests more localised behaviour at the Co atoms and induced behaviour at the Rh atoms.

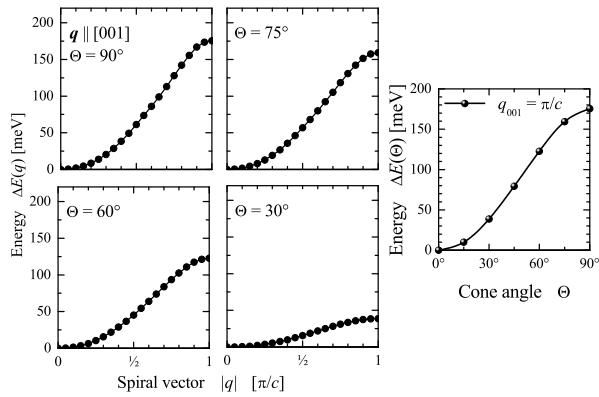


FIG. 5. Conical spirals in Rh_2CoSb . Spiral energies for different cone angles and the wave vector along the c axis ($q||[001]$) are shown. The angular dependence at $q = \pi/c$ is also shown.

The calculated spiral energies indicate that this type of magnetic order is rather improbable. The spiral energies increase monotonously with the wave vector and cone angle, rather independent on the \vec{q} direction. The mono-

tonic behaviour suggests that a canted magnetic order is also very unlikely [16].

3. Exchange coupling and magnons

The exchange coupling energies were calculated using the scheme of Liechtenstein *et al.* [17, 18] to estimate the Curie temperature, spin stiffness, and presence of magnons [12]. The exchange coupling parameters are plotted in Figure 6(a). The most dominant parameters for Co–Co and Co–Rh interactions are shown; all the others are comparatively small. The largest interaction appears for Co atoms in the centre and nearest to the Co in the neighbouring plane. From the calculated exchange coupling energies, the Curie temperature was found to be $T_C = 498$ K, which is close to the experimental value (450 K) [1]. The calculated spin wave stiffness constant is $D_{ij} = 866$ meV·Å², and the interpolation scheme of Padja *et al.* [19] yields an extrapolated spin wave stiffness of $D_0 = 864$ meV·Å².

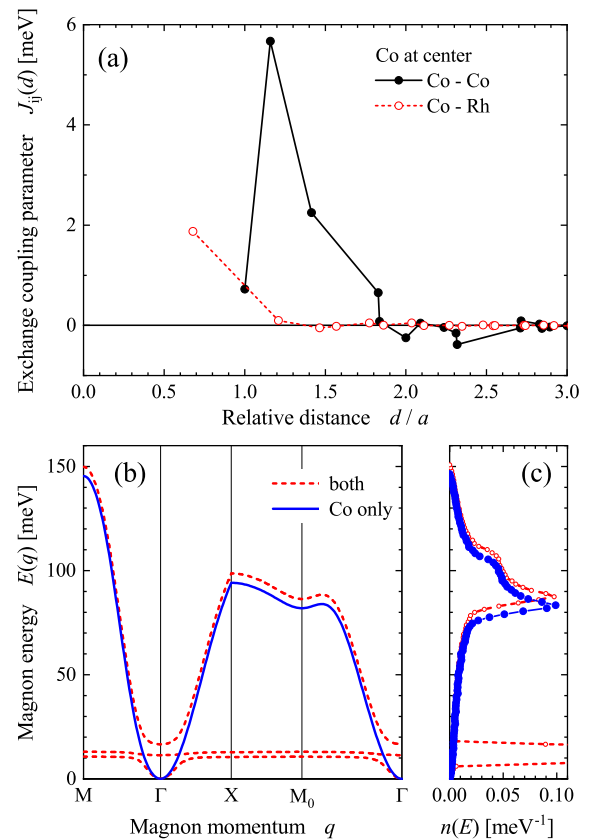


FIG. 6. Exchange coupling parameters of Rh_2CoSb . (a) Exchange coupling parameters for Co–Co and Co–Rh interaction as functions of distance. Lines are drawn for better comparison. (b) Magnon dispersion and (c) density of states. Calculations were performed with and without accounting for the magnetic moment of the Rh atoms (that is, for both atoms and for Co only).

The magnon dispersion was calculated by Fourier transformation of the real space exchange coupling parameters. The result is presented in Figure 6(b), and the magnon density of states is shown in Figure 6(c). Two calculations were made; in one calculation, only the Co–Co interaction was considered, and in the other, the moments of the Rh atoms, which result in additional Co–Rh and Rh–Rh coupling, were included. The latter calculation yields flat dispersion curves and a high density of states. A comparison of the two calculations reveals that the magnons are dominated by the Co–Co interaction. Note that the Curie temperature is only 10 K lower when the Rh moments and the corresponding exchange parameters are ignored.

B. Results for Rh₂FeSb

The calculations for Rh₂FeSb were performed in the same way as for Rh₂CoSb. The regular structure with space group no. 139 was found to be more stable than the inverse structure with space group no. 119. In addition, as in the case of Rh₂CoSb, the calculated c lattice parameter, and thus c/a , are considerably larger than the experimental values (see Table II).

TABLE II. Structural properties of Rh₂FeSb.

Calculations are performed for the regular tetragonal Heusler structures. Lattice parameters (a , c , c/a) and spin magnetic moment m_s of the primitive cell are listed. Experimental values from Reference [1] are shown for comparison. Note that the experimental moments in [1] are not saturated.

	Experiment		
	Calculated	This work	Ref. [1]
a [Å]	4.0418	4.0671	4.07
c [Å]	7.3995	7.0161	6.96
c/a	1.8308	1.7251	1.71
m_s [μ_B]	3.4	3.8	2.8
T_C [K]		510	510

The electronic structure of Rh₂FeSb is illustrated in Figure 7. The fully relativistic band structure and the spin- and site-resolved densities of states are shown. The calculated spin and orbital magnetic moments are $m_s^{\text{Fe}} = 2.978\mu_B$ and $m_l^{\text{Fe}} = 0.080\mu_B$ for iron and $m_s^{\text{Rh}} = 0.228\mu_B$ and $m_l^{\text{Rh}} = 0.006\mu_B$ for rhodium, respectively. The overall magnetic moment (spin plus orbital) of the primitive cell is $m_{\text{tot}} = 3.488\mu_B$. The magnetic moment of the Fe atoms is strongly localised, which is typical of Heusler compounds with high magnetic moments. It clearly exceeds the value for elemental iron.

The real space charge and spin distributions of Rh₂FeSb are shown in Figure 8. As in the Co-containing compound, $\sigma(r)$ does not have a pronounced shape (compare Figure 3). The magnetisation density ($\sigma(r)$) around the Fe atoms has a less distinct shape compared to Co

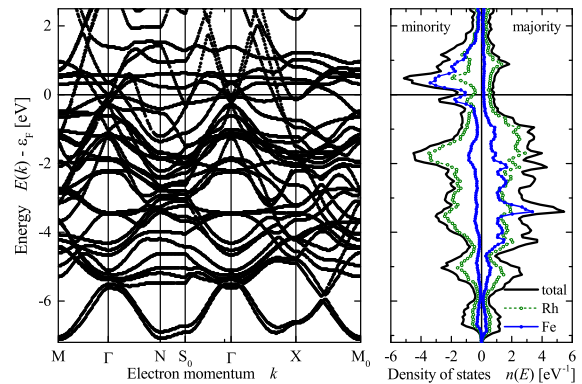


FIG. 7. Electronic structure of Rh₂FeSb (I).

Fully relativistic band structure is shown, along with the total- and site-specific spin-resolved densities of states for Rh and Fe.

in Rh₂CoSb; it is also not greatly affected by changes in the magnetisation direction. The main difference is the magnetisation density around the Rh atoms, which is rotated and appears to be aligned along the magnetisation direction.

Table III compares the calculated magnetic data of Rh₂CoSb and Rh₂FeSb. Rh₂FeSb clearly has a smaller orbital magnetic moment than Rh₂CoSb, whereas its spin magnetic moment is higher because of the effect of the Fe atoms. The induced magnetic moments of the Rh atoms are similar in both compounds.

TABLE III. Calculated magnetic properties of Rh₂FeSb, Rh₂Fe_{0.5}Co_{0.5}Sb, and Rh₂CoSb.

Spin m_s and orbital m_l magnetic moments per atom (Rh, $T = \text{Co, Fe}$ with $m \parallel c$ in all cases) of the primitive cell ($total$) are listed, as well as Curie temperature T_C , spin stiffness D_0 , and anisotropy parameters. (Note that the dipolar anisotropy is three orders of magnitude lower than the magnetocrystalline part.)

	Fe	Fe _{0.5} Co _{0.5}	Co
m_s^{Rh} [μ_B]	0.237	0.239	0.204
m_l^{Rh} [μ_B]	0.006	0.008	0.006
m_s^{Fe} [μ_B]	3.006	2.977	-
m_l^{Fe} [μ_B]	0.080	0.084	-
m_s^{Co} [μ_B]	-	1.747	1.674
m_l^{Co} [μ_B]	-	0.132	0.137
m_s^{total} [μ_B]	3.44	2.81	2.04
m_l^{total} [μ_B]	0.09	0.12	0.15
T_C [K]	465	480	500
D_0 [meV Å ²]	590	700	870
K_u [MJ/m ³]	-1.21	-0.23	1.37
$ \mu_0 H_a $ [T]	1.34	0.31	2.43
$\Delta E_{\text{dipanisotropy}}$ [kJ/m ³]	1.9		2.0

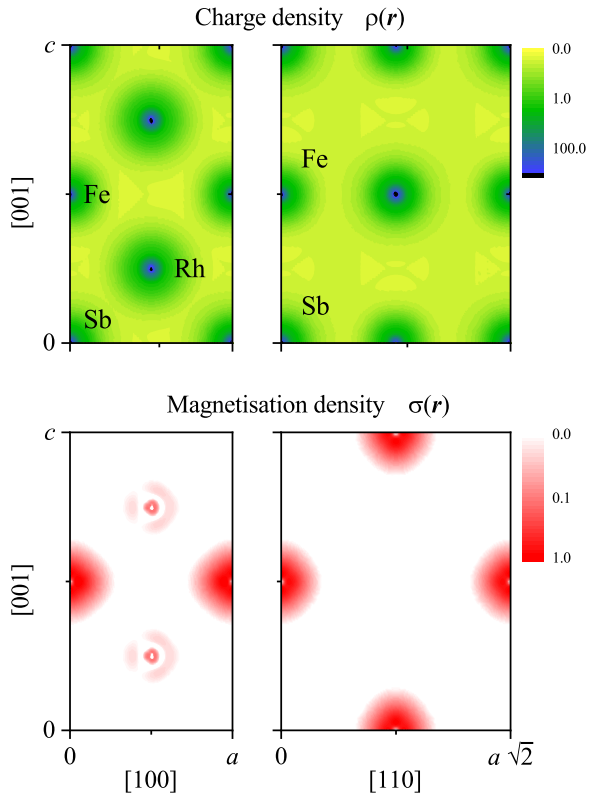


FIG. 8. Electronic structure of Rh_2FeSb (II). Fully relativistic charge ($\rho(r)$) and spin ($\sigma(r)$) distributions for different planes. Magnetisation is perpendicular to c with m along $[100]$ in accordance with the *easy plane* behaviour of the magnetic anisotropy. (Note: colour bars are in atomic units.)

The calculated Curie temperatures are of the same order of magnitude as the experimental values. In contrast to the calculated results, however, the experimental value of the Fe compound is higher than that of the Co compound. A possible reason is differences in the variation of the lattice parameters with temperature, which affect the exchange coupling parameters and thus T_C and also the spin stiffness. Note that a much lower Curie temperature is obtained for the Co compound when it is off-stoichiometric (see Appendix A 2), whereas the T_C value of the off-stoichiometric Fe compound is slightly higher.

The anisotropy has the *hard* axis along the z ($[001]$) direction, and the *easy plane* is the basal plane. By contrast, for Rh_2CoSb , the z direction is the *easy* axis. The simple uniaxial anisotropy constant is $K_u = -1.21 \text{ MJ/m}^3$. Consequently, the anisotropy field is $|\mu_0 H_a| = 1.34 \text{ T}$. The appearance of the “*hard*” axis along z is opposite to Rh_2CoSb where z is the “*easy*” axis. The dipolar magnetocrystalline anisotropy of Rh_2FeSb is $\Delta E_{\text{dipanis}} = 0.09 \mu\text{eV}$, indicating that the *easy* dipolar direction is along the $[001]$ axis, like that of the Co-

containing compound. This behaviour is caused by the strong magnetic moments of the $3d$ transition metals, in addition to the elongation of the tetragonal crystal structure along the c axis.

The dynamic magnetic properties of Rh_2FeSb are shown in Figure 9. The spin spirals and magnons are similar to those of Rh_2CoSb ; however, their energies extend to higher values. The behaviour of the spin spirals rules out the presence of non-collinear magnetic structure [16].

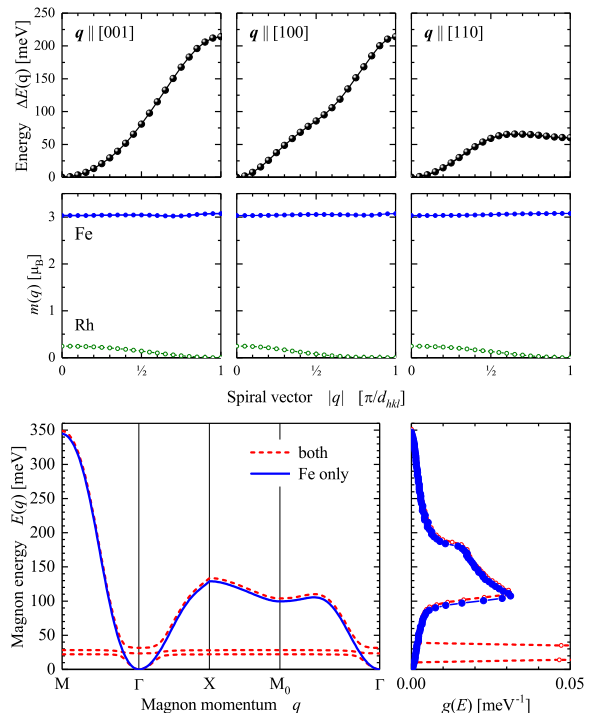


FIG. 9. Dynamic magnetic properties of Rh_2FeSb . Spiral energies with corresponding magnetic moments and the magnon dispersion are shown, along with the magnon density of states $g(E)$. Magnon calculations were performed with and without the magnetic moment of the Rh atoms; in the latter case, all Fe–Rh interactions are neglected.

C. Results for $\text{Rh}_2\text{Fe}_x\text{Co}_{1-x}\text{Sb}$

Owing to the differences in magnetic anisotropy between the Fe- and Co-based compounds, it is interesting to investigate a mixed system containing both Fe and Co. Therefore, calculations were also performed for $\text{Rh}_2\text{Fe}_x\text{Co}_{1-x}\text{Sb}$ using SPRKKR and the CPA. The CPA enables the simulation of random occupation of Fe and Co atoms at a single site (here 2b). The obtained magnetic properties of $\text{Rh}_2\text{Fe}_{0.5}\text{Co}_{0.5}\text{Sb}$ are shown in Table III. The uniaxial anisotropy constant is negative, like that of Rh_2FeSb ; however, its absolute value is considerably lower (by a factor of 35) than that of Rh_2CoSb .

The dependence of the magnetic properties on the composition is shown in Figure 10. The total magnetic moment increases with increasing Fe content, mainly because Fe has a higher spin magnetic moment ($\approx 3 \mu_B$) than Co ($\approx 1.7 \mu_B$). The individual magnetic moments of the atoms are nearly unaffected by the composition. The calculated Curie temperature decreases with increasing Fe content.

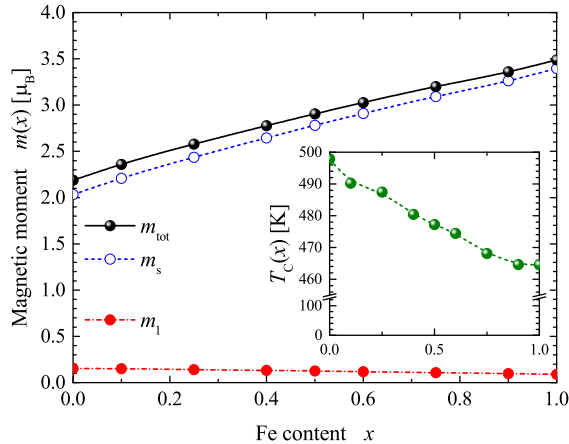


FIG. 10. Magnetic properties of $\text{Rh}_2\text{Fe}_x\text{Co}_{1-x}\text{Sb}$. Total (m_{tot}), spin (m_s), and orbital (m_l) magnetic moments as functions of Fe content x are shown. The inset shows the Curie temperature (T_C).

D. Magnetocrystalline anisotropy of $\text{Rh}_2\text{Fe}_x\text{Co}_{1-x}\text{Sb}$

Thus far, only the simplest case of uniaxial magnetocrystalline anisotropy has been considered. The equations for extending the calculations to more detailed cases are given in Appendix C. These equations were used to calculate the fourth-order uniaxial and tetragonal anisotropy constants, which were used to obtain the magnetocrystalline anisotropy energy distributions.

The calculated uniaxial energy distributions $E_{u'}(\theta, \phi)$ (see Equations (C4) and (C18) in the Appendix) of Rh_2FeSb , $\text{Rh}_2\text{Fe}_{0.5}\text{Co}_{0.5}\text{Sb}$, and Rh_2CoSb are plotted in Figure 11 for comparison.

The different behaviour of the anisotropy is clearly revealed in Figure 11. Rh_2FeSb has an *easy* plane, and c is the *hard* axis; $\text{Rh}_2\text{Fe}_{0.5}\text{Co}_{0.5}\text{Sb}$ has an *easy* plane as well, but a *hard* cone, and in Rh_2CoSb , the c direction is the *easy* axis. $\text{Rh}_2\text{Fe}_{0.5}\text{Co}_{0.5}\text{Sb}$ has a much lower anisotropy than the pure compounds, and the differences between the energies of the ab plane and the c axis are very small. A hard cone appears with its maximum at an angle of $\theta_{3,4} = \pm 35.7^\circ$ (see Equation (C9) in Appendix C 1).

The calculated anisotropy constants for uniaxial and tetragonal symmetry are compared in Table IV. The simple K_u from Equation (C2) (see Appendix C) clearly can-

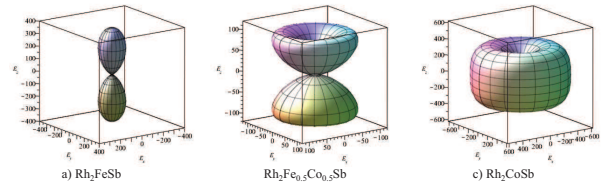


FIG. 11. Uniaxial magnetic anisotropy of Rh_2TSb compounds.

Energy distributions $E_{u'}(\theta, \phi)$ of $T = \text{Fe}$ (a), $\text{Fe}_{0.5}\text{Co}_{0.5}$ (b), and Co (c). The energies $E_{x,y,z}$ are given in μeV . (Please note the different energy scales.)

not describe the magnetic anisotropy correctly.

TABLE IV. Comparison of the anisotropy constants of Rh_2TSb , $T = \text{Fe}$, $\text{Fe}_{0.5}\text{Co}_{0.5}$, and Co .

	Rh_2FeSb	$\text{Rh}_2\text{Fe}_{0.5}\text{Co}_{0.5}\text{Sb}$	Rh_2CoSb
uniaxial			
K_u [MJ/m^3]	-1.21	-0.23	1.37
K_0 [MJ/m^3]	1.31	0.39	0.0
K_2 [MJ/m^3]	-2.19	0.50	3.62
K_4 [MJ/m^3]	0.98	-0.73	-2.25
tetragonal			
$K_{0,0}$ [MJ/m^3]	1.31	0.39	0.0
$K_{2,0}$ [MJ/m^3]	-2.19	0.50	3.62
$K_{4,0}$ [MJ/m^3]	0.93	-0.81	-2.40
$K_{4,4}$ [MJ/m^3]	0.05	0.08	0.15

The dependence of the uniaxial anisotropy constants on the composition is illustrated in Figure 12. The uniaxial anisotropy constant K_u decreases with increasing iron content and exhibits a zero-crossing at $x_0 \approx 0.4$. At intermediate iron contents, more complex behaviour appears, as shown by the composition dependence of K_{2i} and the results in Figures 11 and 13.

The calculated tetragonal energy distributions $E_{a'}(\theta, \phi)$ (see Equations (C12) and (C18) in the Appendix) of Rh_2FeSb , $\text{Rh}_2\text{Fe}_{0.5}\text{Co}_{0.5}\text{Sb}$, and Rh_2CoSb are shown in Figure 13. As in the plot of the uniaxial anisotropy in Figure 11, the differences in the anisotropy are easily observed. In Rh_2FeSb , the *hard* axis is along the z ($[001]$) direction, and the anisotropy exhibits weak variation in the basal plane, which is close to the *easy* plane. Closer examination of the basal plane shows biaxial behaviour with *easy* axes along the $[110]$ and $[\bar{1}\bar{1}0]$ axes, but the energy difference between these directions and the $[100]$ or $[010]$ axes is very small. The anisotropy of Rh_2CoSb is still almost uniaxial, with the *easy* axis along the c ($[001]$) axis, and varies weakly in the basal plane. $\text{Rh}_2\text{Fe}_{0.5}\text{Co}_{0.5}\text{Sb}$ has much lower anisotropy than the pure compounds and exhibits more complicated directional behaviour.

The directional dependence of the orbital magnetic moments was analysed to clarify the role of the spin-

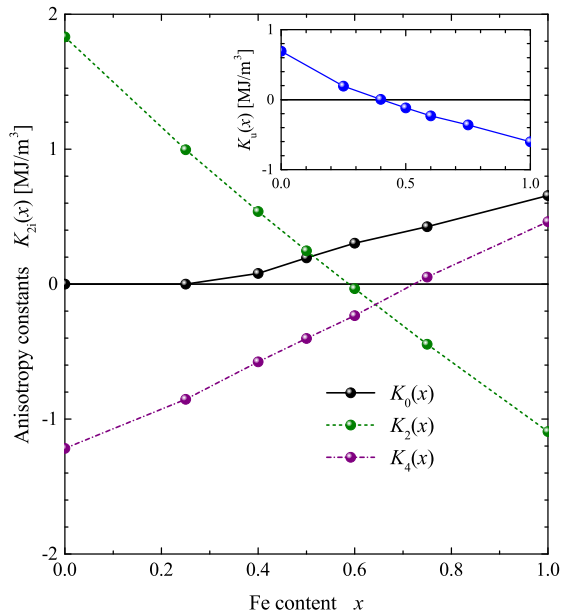


FIG. 12. Anisotropy constants of $\text{Rh}_2\text{Fe}_x\text{Co}_{1-x}\text{Sb}$ compounds. The inset shows the uniaxial anisotropy constant obtained using Equation (C3) in Appendix C 1.

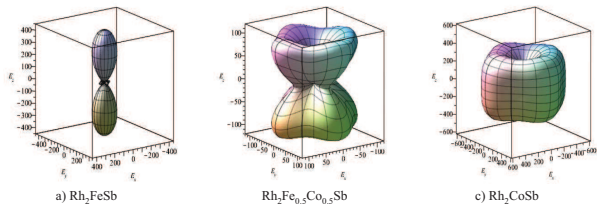


FIG. 13. Tetragonal magnetic anisotropy of Rh_2TSb compounds. Energy distributions $E_{a'}(\theta, \phi)$ of $T = \text{Fe}$ (a), $\text{Fe}_{0.5}\text{Co}_{0.5}$ (b), and Co (c). The energies $E_{x,y,z}$ are given in μeV . (Please note the different energy scales.)

orbit interaction. The magnetic moments for $m\parallel c$ are listed in Table III. The ratio of the total orbital moment to the total spin moment, m_l/m_s , was used owing to the large differences between the magnetic moments for different compositions. Figure 14 shows the ratio m_l/m_s as a function of the difference in the energies in several magnetisation directions $[hkl]$. For both Rh_2CoSb and Rh_2FeSb , the ratio is largest for magnetisation along the c axis ($[001]$) and lowest in the basal plane. This finding involves not only the ratio but also the orbital momenta themselves, indicating that the orbital moment is not always largest when the magnetisation is along the easy axis (or in the easy plane). Here it depends at least partially on the angle between the magnetisation and c axis, as shown by the values for other directions.

To further examine the nature of the anisotropy, the charge and spin density distributions were analysed with

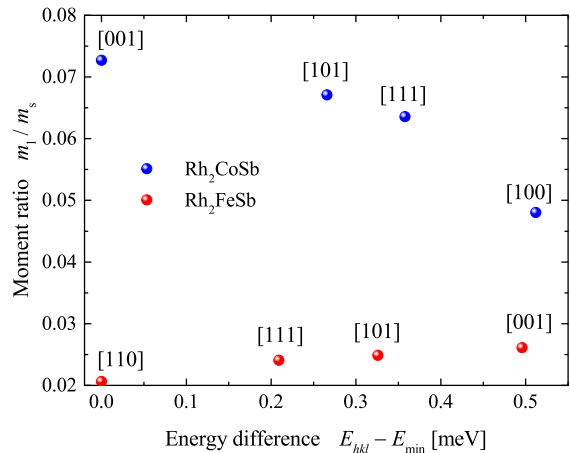


FIG. 14. Directional dependence of the orbital moments of $\text{Rh}_2T'\text{Sb}$, $T' = \text{Co}, \text{Fe}$. Note that the orbital moments are given relative to the spin moments for better comparison.

respect to the magnetisation direction (compare also Figures 3 and 8). As mentioned above, the symmetry changes when the magnetisation is applied along different crystallographic directions. The point group symmetry of the 2b sites occupied by Fe and Co is D_{4h} and D_{2d} for Rh on 4d. Applying the magnetisation along one of the high-symmetry axes, i.e., the c ($[001]$) or a ($[100]$) axis, changes the symmetry of the 2b sites to C_{4h} or C_{2h} , respectively. As a result, the irreducible representations and basic functions depend on the magnetisation direction. For C_{4h} , they are a_g , b_g , and e_g with the $l = 2$ basic functions d_{z^2} , $(d_{x^2-y^2}, d_{xy})$, and (d_{xz}, d_{yz}) . For C_{2h} , they are a_g and b_g with $(d_{z^2}, d_{x^2-y^2}, d_{xy})$ and (d_{xz}, d_{yz}) . Similar differences appear for the 4d sites. The charge and spin density distributions for different magnetisation directions are compared in Figure 15 for the compounds containing only Fe or Co.

As mentioned above, the details of the charge density are not easily observed directly from the graph when the magnetisation direction is changed, because the graph shows mainly the positions of the atoms. However, they can be observed if one investigates the difference in the charge distribution, which is plotted as $\Delta\rho(r)$. It was calculated for both compounds as the difference between the charge densities obtained assuming that the magnetisation is parallel ($m\parallel[001]$) or perpendicular ($m\parallel[100]$) to the c axis. In both compounds, the magnetisation has the same effect on $\Delta\rho(r)$ near the Rh atoms. That is, the charge distribution is rotated with the direction of the magnetisation. In the same way, the Rh-based spin densities are affected by the magnetisation direction. They change from $[001]$ -aligned when $m\parallel[001]$ to $[100]$ -aligned when $m\parallel[100]$, regardless of which 3d transition metal is used. The situation is different near the 3d transition metals Fe and Co, where $\Delta\rho(r)$ and $\sigma(r)$ are affected very differently by the magnetisation direction. The rea-

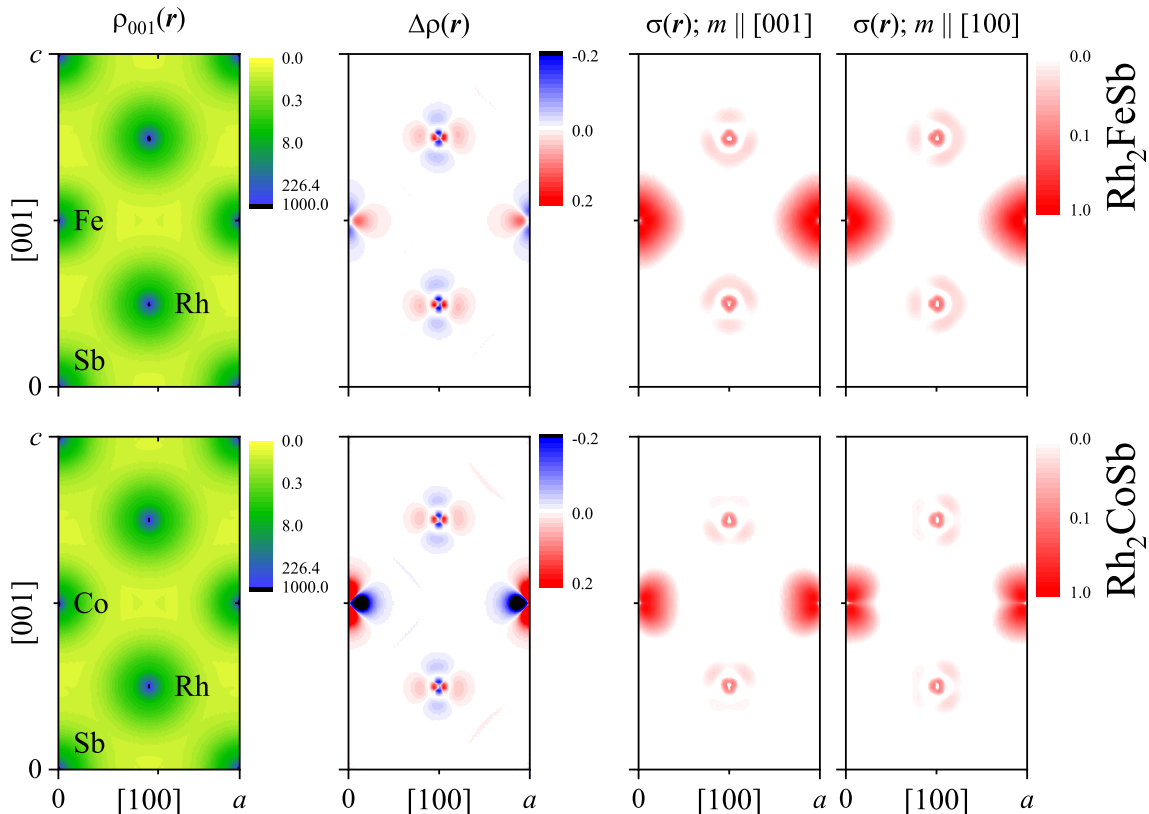


FIG. 15. Electronic structure of Rh_2FeSb and Rh_2CoSb .

Fully relativistic charge ($\rho(r)$) and spin ($\sigma(r)$) density distributions in a (100)-type plane for magnetisation parallel and perpendicular to the c axis are shown. $\rho_{001}(r)$ is the charge density for $m \parallel [001]$, and $\Delta\rho = \rho_{001} - \rho_{100}$ is the difference between the charge densities for $m \parallel [001]$ and $m \parallel [100]$. (Note: colour bars are in atomic units.)

son is the different occupation of $3d$ valence electrons of Fe ($n_d^{\text{Fe}} = 6.6$) and Co ($n_d^{\text{Co}} = 7.8$), which are responsible for the different spin moments. The overall differences in the charge and spin densities at different magnetisation directions result in different total energies.

Finally, the gain or loss of energy with changes in the magnetisation direction results in the magnetocrystalline anisotropy. The electronic structure of the two compounds, Rh_2FeSb and Rh_2CoSb , differs depending on the magnetisation direction, which is reflected in the change in the anisotropy from the easy plane to the easy axis when Fe is replaced with Co.

IV. CONCLUSIONS

The electronic and magnetic structure of tetragonal Heusler compounds with the composition $\text{Rh}_2\text{Fe}_x\text{Co}_{1-x}\text{Sb}$ were investigated by *ab initio* calculations. The calculations revealed that the magnetic moment increases and the Curie temperature decreases with increasing Fe content x . The Rh atoms have only

small, composition-independent magnetic moments. The magnetic properties are determined by those of the Fe and Co atoms and thus depend strongly on the composition. The total energies for various magnetisation directions were calculated to determine the magnetic anisotropy. The analysis is described in detail in an extended Appendix. For bulk materials, the magnetocrystalline anisotropy is found to be much stronger (by three orders of magnitude) than the dipolar anisotropy. Special attention was given to the borderline compounds, Rh_2FeSb and Rh_2CoSb . The most striking result was that a composition-dependent transition from easy-axis to easy-plane anisotropy occurs at an iron concentration of approximately 40%.

Appendix A: Disorder

1. Rh_2CoSb with Co–Sb-type antisite disorder

Supplementary calculations were performed for disordered Rh_2CoSb and Rh_2FeSb using SPRKKR us-

ing the coherent potential approximation. For example, the disordered compound may be written as $\text{Rh}_2(\text{Co}_{1-x/2}\text{Sb}_{x/2})(\text{Co}_{x/2}\text{Sb}_{1-x/2})$, where x is the disorder level. The result for $x = 1$, which denotes complete Co–Sb disorder, is illustrated in Figure 1(b). Alternatively, it can be assumed that disorder between the Co and Rh atoms decreases the magnetic moments, which is consistent with the results of calculations of the inverted structure in space group 119, but not with those when Co–Sb disorder is assumed, as shown below.

The evolution of the magnetic moments of Rh_2CoSb and Rh_2FeSb with increasing disorder is shown in Figure 16. The total magnetic moment in the fully disordered state is approximately 20% larger for Rh_2CoSb and approximately 10% larger for Rh_2FeSb than those of the compounds in the completely ordered state. The orbital moments are nearly constant in both compounds and are independent of the degree of disorder (x). The decrease in the total moments with decreasing x is attributed to the decrease in the spin magnetic moments of both compounds.

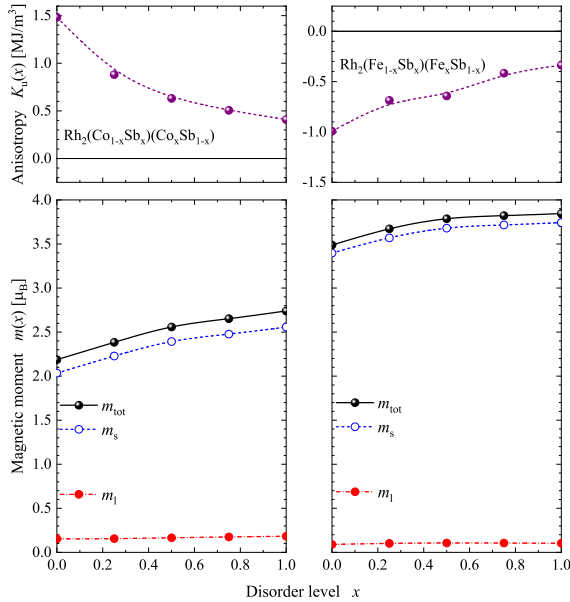


FIG. 16. Disorder-induced changes in magnetic moments and anisotropy of $\text{Rh}_2(T_{1-x/2}\text{Sb}_{x/2})(T_{x/2}\text{Sb}_{1-x/2})$ $T = \text{Co}, \text{Fe}$. Total, spin, and orbital magnetic moments are shown, along with the uniaxial anisotropy constant K_u as a function of disorder level x .

Figure 16 shows that the type of anisotropy (easy axis for Rh_2CoSb and easy plane for Rh_2FeSb) is retained even in the completely disordered state. However, the absolute value of the second-order uniaxial anisotropy constant K_u decreases. That is, the anisotropy becomes weaker with increasing disorder. The K_u values of both compounds are approximately 70% higher in the completely disordered state. No direct correspondence is observed between the behaviour of K_u and that of the

spin, orbital, or total magnetic moments. The effects of disorder and composition on the magnetic anisotropy of the Co–Fe system were investigated using first principles CPA calculations by Turek *et al.* [20], who also observed a decrease in anisotropy with increasing disorder.

2. Off-stoichiometric alloys

In many experiments, 2:1:1 stoichiometry was not fully reached, but an excess of Fe or Co and a deficiency of Sb was obtained. In particular, the magnetic properties of $\text{Rh}_2T_{1+x}\text{Sb}_{1-x}$, with $T = \text{Fe}, \text{Co}$, were calculated for $x = 0.12$. As in the study of disorder, the calculations were performed using the CPA. The $2a$ site is assumed to be occupied by 12% with Fe (or Co) and by 88% with Sb, whereas the occupations of the $4d$ and $2b$ sites are unchanged.

The calculated magnetic properties of the off-stoichiometric alloys are listed in Table V. The magnetic moments and spin stiffness D_0 are enhanced in both alloys, and the values are higher than those of the stoichiometric compound. In particular, the excess Co and Fe atoms on the $2a$ site contribute a large spin moment. The total magnetic moment, $m_s + m_l = 2.627 \mu_B$, of $\text{Rh}_2\text{Co}_{1.12}\text{Sb}_{0.88}$ is very similar to the experimentally observed value of $2.6 \mu_B$. The Curie temperature of the off-stoichiometric Co-containing compound is slightly lower, whereas that of the Fe compound is slightly higher. These findings, along with the spin stiffness results, suggest that the exchange coupling parameters of the stoichiometric compounds differ from those of the off-stoichiometric alloys.

The type of anisotropy (easy plane or easy axis) is the same in the off-stoichiometric alloys as in the stoichiometric compounds. The uniaxial anisotropy constants differ, however. They are enhanced in the Fe alloy and reduced in the Co alloy.

Appendix B: Semi-relativistic band structures

The semi-relativistic band structures of Rh_2FeSb and Rh_2CoSb are compared in Figure 17 to illustrate the spin characteristics of the bands. The band structures are similar; the main differences result from the larger band filling in the Co-based compound, which has one more valence electron than the Fe compound. Further, the larger spin splitting in the Fe compound clearly results in a large spin magnetic moment.

Appendix C: Magnetocrystalline anisotropy

In this Appendix, the discussion of the magnetocrystalline anisotropy is extended beyond simple uniaxial approximations. The magnetocrystalline energy of uniaxial

TABLE V. Calculated magnetic properties of off-stoichiometric $\text{Rh}_2\text{T}_{1.12}\text{Sb}_{0.88}$.

Spin m_s and orbital m_l magnetic moments per atom (Rh, Co, Fe) and those of the primitive cell (*total*) are listed, as well as the Curie temperature T_C and spin stiffness D_0 . $m_{s,l}^{2b}$ represents the magnetic moments at the original position, and $m_{s,l}^{2a}$ represents the moments of the excess Fe and Co atoms at the initial Sb position.

$\text{Rh}_2\text{T}_{1.12}\text{Sb}_{0.88}$	$T = \text{Fe}$	$T = \text{Co}$
$m_s^{\text{Rh}} [\mu_B]$	0.308	0.244
$m_l^{\text{Rh}} [\mu_B]$	0.012	0.009
$m_s^{2b} [\mu_B]$	2.988	1.691
$m_l^{2b} [\mu_B]$	0.092	0.140
$m_s^{2a} [\mu_B]$	3.564	2.521
$m_l^{2a} [\mu_B]$	0.072	0.155
$m_s^{\text{total}} [\mu_B]$	4.010	2.453
$m_l^{\text{total}} [\mu_B]$	0.124	0.174
T_C [K]	490	480
D_0 [meV \AA^2]	690	1100
K_u [MJ/m ³]	-1.667	0.826

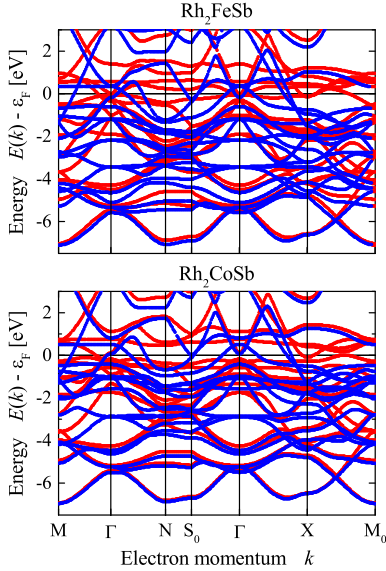


FIG. 17. Semi-relativistic band structures of Rh_2FeSb and Rh_2CoSb . Red and blue indicate majority and minority states, respectively.

systems can be derived from the first principles total energies for different magnetisation directions (quantisation axes).

Textbooks give different descriptions of the magnetic anisotropy, in particular, different equations for the anisotropy constants [21–26]. Therefore, care must be taken when comparing the results of this work with those of other studies or comparing other studies with each

other.

1. Uniaxial magnetic anisotropy

It is often assumed that the magnetocrystalline anisotropy in tetragonal or hexagonal systems is simply described by a second-order dependence on the angle θ between the c axis and the magnetisation direction, that is,

$$K_u \sin^2(\theta), \quad (\text{C1})$$

where K_u is the uniaxial anisotropy constant. In that case,

$$K_u = E^{100} - E^{001} \quad (\text{C2})$$

is simply calculated from the difference between the energies for magnetisation along the principal axes, $c \parallel [001]$ and $a \parallel [100]$. For $K_u > 0$, the *easy* axis is along the c axis, whereas $K_u < 0$ describes an *easy* plane where c is the *hard* axis. For a distinct magnetic anisotropy in the ab plane, it would be more accurate to use the lowest energy of the two in-plane directions along the principal axis and the diagonal, which are the $[100]$ and $[110]$ directions, respectively:

$$K_u = \min(E^{100}, E^{110}) - E^{001}. \quad (\text{C3})$$

Equation (C1) has another serious drawback; namely, the anisotropy is completely independent of the crystal lattice, and the anisotropic energy distribution always has the same shape regardless of the c/a parameter and whether the crystal has tetragonal, hexagonal, or some other structure. That is, Equation (C1) is ultimately useful only for distinguishing between *easy* and *hard* c axes.

Now we consider only tetragonal systems. By using the series expansion $\sum K_{2\nu,0} \sin^{2\nu}(\theta)$ up to the fourth order in $\sin(\theta)$, the uniaxial magnetocrystalline energy is expressed as

$$E_{\text{crys}}^{\text{uniaxial}} = K_0 + K_2 \sin^2(\theta) + K_4 \sin^4(\theta). \quad (\text{C4})$$

The equations for the sixth-order uniaxial anisotropy are discussed by Jensen and Bennemann [27], for example. In the following, the subscript "crys" is omitted, and the energies are indexed only by direction or by "uni". For the high-symmetry directions $[h, k, l]$ and the lowest indices ($h, k, l = 0, 1$), the energies depend on the anisotropy coefficients as follows:

$$\begin{aligned}
E^{001} &= K_0, \\
E^{100} &= K_0 + K_2 + K_4, \text{ or} \\
E^{110} &= K_0 + K_2 + K_4, \text{ and} \\
E^{101} &= K_0 + K_2 \sin^2(\theta^{101}) + K_4 \sin^4(\theta^{101}), \text{ or} \\
E^{111} &= K_0 + K_2 \sin^2(\theta^{111}) + K_4 \sin^4(\theta^{111}).
\end{aligned} \tag{C5}$$

Note that the energies for the [100] and [110] directions are identical only when uniaxial anisotropy is assumed. The energies for the [101] and [111] directions, however, have different angles with respect to the c axis. From Equations (C4 and C5), K_2 and K_4 may be obtained, for example, from the differences:

$$\begin{aligned}
E^{100} - E^{001} &= K_2 + K_4 \text{ and} \\
E^{101} - E^{001} &= K_2 \sin^2(\theta) + K_4 \sin^4(\theta).
\end{aligned} \tag{C6}$$

For $z = c/a$, the angle θ is found using $\theta^{101} = \theta^{011} = \arctan(1/z)$. From Equation (C5) or (C6), the anisotropy constants K_i are given by

$$\begin{aligned}
K_0 &= E^{001}, \\
K_2 &= (E^{101} - E^{001})(z^2 + 2) + (E^{101} - E^{100})\frac{1}{z^2}, \\
K_4 &= (E^{001} - E^{101})(z^2 + 1) + (E^{100} - E^{101})\frac{(z^2 + 1)}{z^2}.
\end{aligned} \tag{C7}$$

Alternatively, E^{111} and $\theta^{111} = \arctan(\sqrt{2}/z)$ may be used, but the resulting equations will have a different dependence on c/a . The uniaxial magnetocrystalline anisotropy energy (E_u) is the difference between the magnetocrystalline energy (here E^{uni}) and the isotropic contribution, which is the spherical part K_0 :

$$E_u = E^{\text{uni}} - K_0. \tag{C8}$$

According to this equation, the uniaxial magnetocrystalline anisotropy energy may be positive or negative, depending on the directions and values of K (see also Appendix C4).

Equation (C4) has four extremal values at

$$\theta_i = 0, \frac{\pi}{2}, \text{ and } \pm \arcsin\left(\sqrt{\frac{-K_2}{2K_4}}\right), \tag{C9}$$

where the first derivative of the fourth-order equation [Equation (C4)] vanishes, that is, for $dE^{\text{uniaxial}}/d\theta = 0$. The solutions $\theta_{3,4}$ are real only if the anisotropy constants obey the relation $0 \leq \frac{-K_2}{2K_4} \leq 1$, that is, $K_2K_4 \geq 0$, $|K_2| \leq 2|K_4|$. For $K_2 = -2K_4$, one has $\theta_{3,4} = \pm 90^\circ$. For a real $\theta_{3,4}$, one has an *easy* or a *hard* cone. The resulting extremal energies are

$$\begin{aligned}
E(0) &= K_0, \\
E(\pi/2) &= K_0 + K_2 + K_4, \\
E(\theta_{3,4}) &= K_0 - \frac{K_2^2}{4K_4}.
\end{aligned} \tag{C10}$$

The minima or maxima are obtained using the second derivatives of the energy at the extremal angles:

$$\begin{aligned}
\left.\frac{d^2E}{d\theta^2}\right|_0 &= 2K_2, \\
\left.\frac{d^2E}{d\theta^2}\right|_{\pi/2} &= -2(K_2 + 2K_4), \\
\left.\frac{d^2E}{d\theta^2}\right|_{\theta_{3,4}} &= -\frac{2K_2(K_2 + 2K_4)}{K_4}.
\end{aligned} \tag{C11}$$

The minima appear for positive 2nd derivatives ($d^2E/d\theta^2|_{\theta_i} > 0$) and define the easy direction(s) of magnetisation. Indeed, one has to search for the absolute minimum and maximum to find the correct easy and hard axes, planes, or cones. An easy cone appears for $K_2 < 0$, $K_4 > -K_2/2$, and the corresponding cone angle is given by $\theta_{3,4}$. A special hard cone exists for $K_2 > 0$, $K_4 = -K_2$, where both the c axis and the ab plane have the same (lowest) energy. The energy barrier at the hard cone must be overcome, however, to change the magnetisation direction from the easy axis to the easy plane and vice versa. In the range $-\infty < K_4 < -K_2/2$, the solutions are metastable when $K_2 > 0$. The complete fourth-order uniaxial anisotropy phase diagram is presented in Table VI.

TABLE VI. Uniaxial anisotropy phase diagram. ab stands for basal plane, c stands for c -axis. Cones may have an opening angle θ or $\pi/4$ with respect to the c axis.

K_2	K_4	easy	hard
> 0	$-\infty \dots -K_2$	ab	cone (θ)
> 0	$-K_2$	ab, c	cone (45°)
> 0	$-K_2 \dots -K_2/2$	c	cone (θ)
> 0	$-K_2/2 \dots \infty$	c	ab
$= 0$	$= K_2 = 0$	undefined, spherical	
< 0	$-K_2 \dots \infty$	cone (θ)	ab
< 0	$-K_2$	cone (45°)	ab, c
< 0	$-K_2/2 \dots -K_2$	cone (θ)	c
< 0	$-\infty \dots -K_2/2$	ab	c

The magnetic anisotropy phase diagram for fourth-order uniaxial anisotropy is displayed in Figure 18. It is similar to the graphical representations reported in References [27, 28]. The different phases are distinguished. For $K_4 = -K_2 < 0$, there is a distinct metastable case with equal energies for magnetisation along the c axis and in

the ab plane. At this line, a transition occurs from easy-axis to easy-plane behaviour. In the metastable region for $K_4 < -K_2/2 < 0$, easy-axis behaviour appears, whereas easy-plane behaviour appears for $K_4 < -K_2 < 0$ (see Table VI). In both cases, the sizes of the anisotropy constants determine how easily one state can switch to the other and the stability of the state with lower energy. The energy barrier to cross the hard cone has a size of $-\frac{K_2^2}{4K_4}$, as mentioned above.

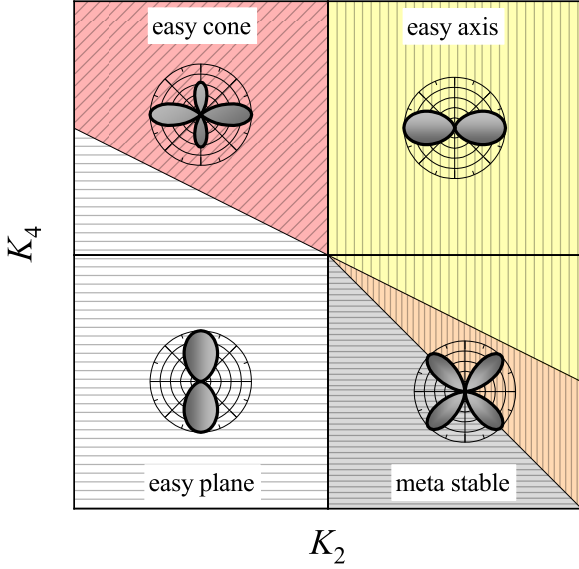


FIG. 18. Magnetic anisotropy phase diagram. In the *metastability* range, *hard-cone*-type anisotropy occurs. In the sketches of the $E(\theta)$ distributions, it is assumed that $K_0 = 0$.

2. Tetragonal magnetic anisotropy

The uniaxial magnetic anisotropy does not reflect the symmetry of the crystal structure. The symmetry of the anisotropy should generally be the same as the symmetry of the crystal potential; thus, it is given by the fully symmetric irreducible representation of the point group, that is, a , a_1 , a_g , or similar. Again, by using a series expansion up to the fourth order in $\sin(\theta)$, the magnetocrystalline energy of a tetragonal system is expressed as

$$\begin{aligned} E_{\text{crys}}^{\text{tetragonal}} &= \sum_{\nu=0}^2 K_{2\nu,0} \sin^{2\nu}(\theta) + K_{4,4} \sin^4(\theta) f(\phi), \\ &= E_{\text{crys}}^{\text{uniaxial}} + K_{4,4} \sin^4(\theta) f(\phi), \\ f(\phi) &= \cos(4\phi). \end{aligned}$$

$f(\phi)$ has an azimuthal dependence on 4ϕ , which results in the expected fourfold symmetry. Some works

used $f'(\phi) = \sin^4(\phi) + \cos^4(\phi)$, which results in different equations and K values. Higher-order approximations will include terms with $K_{6,0}$, $K_{6,4}$, $K_{8,0}$, $K_{8,4}$, $K_{8,8}$, and so on. Subtracting K_0 from Equation (C12) yields

$$E_a(\vec{r}) = K_{2,0} \sin^2(\theta) + [K_{4,0} + K_{4,4} \cos(4\phi)] \sin^4(\theta). \quad (\text{C12})$$

In the following, the subscript "crys" is omitted, and the energies are indexed only by direction or by "tet". For the high-symmetry directions $[h, k, l]$ and the lowest indices $(h, k, l = 0, 1)$, Equation (C12) gives

$$\begin{aligned} E^{001} &= K_{0,0}, \\ E^{100} &= K_{0,0} + K_{2,0} + K_{4,0} + K_{4,4}, \\ E^{110} &= K_{0,0} + K_{2,0} + K_{4,0} - K_{4,4}, \text{ and} \\ E^{101} &= \sum_{\nu=0,2} K_{2\nu,0} \sin^{2\nu}(\theta^{101}) + K_{4,4} \sin^4(\theta^{101}), \text{ or} \\ E^{111} &= \sum_{\nu=0,2} K_{2\nu,0} \sin^{2\nu}(\theta^{111}) - K_{4,4} \sin^4(\theta^{111}). \end{aligned} \quad (\text{C13})$$

For $z = c/a$, the angle θ^{101} is found using $\theta^{101} = \theta^{011} = \arctan(1/z)$. Alternatively, E^{111} with $\theta^{111} = \arctan(\sqrt{2}/z)$ may be used. From the first four energies of Equation (C13), the anisotropy constants $K_{l,m}$ are found to be

$$\begin{aligned} K_{0,0} &= E^{001}, \\ K_{2,0} &= (E^{101} - E^{001})(z^2 + 2) \\ &\quad + (E^{101} - E^{100}) \frac{1}{z^2}, \\ K_{4,0} &= (E^{001} - E^{101})(z^2 + 1) \\ &\quad + (E^{100} - E^{101}) \frac{1}{z^2} \\ &\quad + \frac{1}{2}(E^{100} + E^{110} - 2E^{101}), \\ K_{4,4} &= \frac{1}{2}(E^{100} - E^{110}). \end{aligned} \quad (\text{C14})$$

The magnetocrystalline anisotropy energy (E_a) is the difference between the magnetocrystalline energy (here E^{tet}) and the isotropic contribution, which is the spherical part K_0 :

$$E_a = E^{\text{tet}} - K_0. \quad (\text{C15})$$

3. Dipolar magnetic anisotropy

In non-cubic systems, the dipolar anisotropy does not vanish and also contributes to the magnetocrystalline anisotropy. It is calculated from a direct lattice sum yielding the dipolar energy:

$$E_{dip}(\vec{n}) = \frac{\mu_0}{8\pi} \sum_{i \neq j} \left[\frac{\vec{m}_i \cdot \vec{m}_j}{r_{ij}^3} - 3 \frac{(\vec{r}_{ij} \cdot \vec{m}_i)(\vec{r}_{ij} \cdot \vec{m}_j)}{r_{ij}^5} \right], \quad (\text{C16})$$

where $\vec{n} = \vec{M}/M$ is the magnetisation direction, and r_{ij} represents the distance vectors between the magnetic moments m_i and m_j . The individual magnetic moments, \vec{m}_i and \vec{m}_j , do not necessarily have to be collinear in general.

In a simplified picture, only the 3d transition elements T carry a significant magnetic moment in the Rh_2TSb compounds investigated here. In all cases of a single magnetic ion where all the magnetic moments in the structure are collinear along \vec{n} , the equation simplifies to

$$\begin{aligned} E_{dip}(\vec{n}) &= \frac{\mu_0 m^2(\vec{n})}{8\pi} \sum_{i \neq j} \frac{1}{r_{ij}^3} \left[1 - 3 \frac{r_{n,ij}^2}{r_{ij}^2} \right], \\ &= \frac{\mu_0 m^2(\vec{n})}{8\pi} \sum_{i \neq j} \frac{1 - 3 \cos^2(\theta_{ij})}{r_{ij}^3}, \end{aligned} \quad (\text{C17})$$

where $r_{n,ij} = r_{n,ij}(\vec{n})$ is a projection of the position vector onto the direction of the magnetic moment, and θ_{ij} is the angle between them. In Equation (C17), the sign of the energy is completely defined by the crystal structure when the summation is over a spherical particle. Note that the size of the magnetic moment, $m(\vec{n})$, depends on the magnetisation direction when the spin-orbit interaction is taken into account.

Finally, the dipolar anisotropy is given by the difference between the energies for two different directions,

$\Delta E_{\text{dip aniso}} = E(\vec{n}_2) - E(\vec{n}_1)$. Again, the two well-distinguished directions are the $\vec{n}_1 = [001]$ and $\vec{n}_2 = [100]$ directions, which are along the c axis and in the basal plane along a , respectively. Positive values indicate an easy dipolar direction that is along the $[001]$ axis. It has a second-order angular dependence.

4. Plotting the magnetic anisotropy

According to Equations (C8) and (C15), the magnetocrystalline anisotropy energy may be positive or negative, depending on the direction of (θ, ϕ) and the K values. Consequently, it is difficult to visualise the anisotropy energy by plotting the three-dimensional distribution of $E_a(\vec{r}) = E_a(\theta, \phi)$. Therefore, the alternative anisotropy energy $E_{a'}$ with respect to the lowest energy is generally plotted, where

$$E_{a'} = E_a - \min(E_a), \quad (\text{C18})$$

which is still positive even when $E_a < 0$. The easy directions or planes are identified as those for which $E_{a'} = 0$. $E_{a'}$ is used to plot the magnetocrystalline anisotropy in the main text.

ACKNOWLEDGMENTS

We thank the groups of P. Blaha (Vienna) and H. Ebert (Munich) for providing their computer codes.

-
- [1] S. K. Dhar, A. K. Grover, S. K. Malik, and R. Vijayaraghavan, Peaks in low field a.c. susceptibility of ferromagnetic Heusler alloys, *Sol. St. Comm.* **33**, 545 (1980).
 - [2] S. V. Faleev, Y. Ferrante, J. Jeong, M. G. Samant, B. Jones, and S. S. P. Parkin, Heusler compounds with perpendicular magnetic anisotropy and large tunneling magnetoresistance, *Phys. Rev. Materials* **1**, 024402 (2017).
 - [3] P. Blaha, K. Schwarz, P. Sorantin, and S. B. Trickey, Full-potential, linearized augmented plane wave programs for crystalline systems, *Comput. Phys. Commun.* **59**, 399 (1990).
 - [4] K. Schwarz and P. Blaha, Solid state calculations using WIEN2k, *Comput. Mater. Sci.* **28**, 259 (2003).
 - [5] P. Blaha, K. Schwarz, G. K. H. Madsen, D. Kvasnicka, and J. Luitz, *WIEN2k: An Augmented PlaneWave + Local Orbitals Program for Calculating Crystal Properties* (Wien, 2013).
 - [6] H. Ebert, Fully relativistic band structure calculations for magnetic solids - formalism and application, in *Electronic Structure and Physical Properties of Solids. The Use of the LMTO Method*, Lecture Notes in Physics, Vol. 535, edited by H. Dreyse (Springer-Verlag, Berlin, Heidelberg, 1999) pp. 191 – 246.
 - [7] H. Ebert, D. Ködderitzsch, and J. Minar, Calculating condensed matter properties using the KKR-Greens function method – recent developments and applications, *Rep. Prog. Phys* **74**, 096501 (2011).
 - [8] J. P. Perdew, K. Burke, and M. Ernzerhof, Generalized Gradient Approximation Made Simple, *Phys. Rev. Lett.* **77**, 3865 (1996).
 - [9] H. C. Kandpal, G. H. Fecher, and C. Felser, Calculated electronic and magnetic properties of the half-metallic, transition metal based Heusler compounds, *J. Phys. D: Appl. Phys.* **40**, 1507 (2007).
 - [10] G. H. Fecher, S. Chadov, and C. Felser, Theory of the half-metallic heusler compounds, in *Spintronics*, edited by C. Felser and G. H. Fecher (Springer Verlag, Dordrecht Heidelberg New York London, 2013) Book section 7, p. 115.
 - [11] S. Mankovsky, G. H. Fecher, and H. Ebert, Electronic structure calculations in ordered and disordered solids with spiral magnetic order, *Phys. Rev. B* **83**, 144401 (2011).
 - [12] J. Thoene, S. Chadov, G. Fecher, C. Felser, and J. Kübler, Exchange energies, Curie temperatures and

- magnons in Heusler compounds, *J Phys. D: Appl. Phys.* **42**, 084013 (2009).
- [13] P. Soven, Coherent-Potential Model of Substitutional Disordered Alloys, *Phys. Rev.* **156**, 809 (1967).
- [14] S. A. Khan, P. Blaha, H. Ebert, J. Minar, and O. Siper, Magnetocrystalline anisotropy of FePt: A detailed view, *Phys. Rev. B* **94**, 144436 (2016).
- [15] S. J. Joshua, *Symmetry principles and magnetic symmetry in solid state physics*. (Adam Hilger, IOP Publishing Ltd., Bistol, Philadelphia, New York, 1991).
- [16] R. Lizarraga, L. Nordström, L. Bergqvist, A. Bergman, E. Sjöstedt, P. Mohn, and O. Eriksson, Conditions for Noncollinear Instabilities of Ferromagnetic Materials, *Phys. Rev. Lett.* **93**, 107205 (2004).
- [17] A. I. Liechtenstein, M. I. Katsnelson, and V. A. Gubanov, Exchange interactions and spin-wave stiffness in ferromagnetic metals, *J. Phys. F: Met. Phys.* **14**, L125 (1984).
- [18] A. I. Liechtenstein, M. I. Katsnelson, V. P. Antropov, and V. A. Gubanov, Local Spin Density Functional Approach to the Theory of Exchange Interactions in Ferromagnetic Metals and Alloys, *J. Magn. Magn. Mater.* **67**, 65 (1987).
- [19] M. Pajda, J. Kudrnovsky, I. Turek, V. Drchal, and P. Bruno, Ab initio calculations of exchange interactions, spin-wave stiffness constants, and Curie temperatures of Fe, Co, and Ni, *Phys. Rev. B* **64**, 174402 (2001).
- [20] I. Turek, J. Kudrnovsky, and K. Carva, Magnetic anisotropy energy of disordered tetragonal Fe-Co systems from ab initio alloy theory, *Phys. Rev. B* **86**, 174430 (2012).
- [21] R. Skomsky and J. M. D. Coey, *Permanent Magnetism*, Studies in Condensed Matter Physics (Taylor and Francis Group, New York, 1999).
- [22] J. Kübler, *Theory of Itinerant Electron Magnetism* (Clarendon Press, Oxford, 2000).
- [23] B. D. Cullity and C. D. Graham, *Introduction to Magnetic Materials; 2nd Ed.* (John Wiley and Sons, Hoboken, 2009).
- [24] J. M. D. Coey, *Magnetism and Magnetic Materials* (Cambridge University Press, Cambridge, 2010).
- [25] N. A. Spaldin, *Magnetic Materials, 2nd Ed. Fundamentals and Applications* (Cambridge University Press, Cambridge, 2011).
- [26] K. M. Krishnan, *Fundamentals and Applications of Magnetic Materials* (Oxford University Press, Oxford, 2016).
- [27] P. J. Jensen and K. H. Bennemann, Magnetic structure of films: Dependence on anisotropy and atomic morphology, *Srf. Sci Rep.* **61**, 129 (2006).
- [28] R. Skomski, H.-P. Oepen, and J. Kirschner, Unidirectional anisotropy in ultrathin transition-metal films, *Phys. Rev. B* **58**, 11138 (1998).